LAWRENCE
LIVERMORE
NATIONAL
LABORATORY

LLNL-JRNL-400737

Post-Treatment Hemodynamics of a Basilar Aneurysm and Bifurcation

J. Ortega, J. Hartman, J. Rodriguez, D. Maitland

January 25, 2008

Annals of Biomedical Engineering

Disclaimer

Post-Treatment Hemodynamics of a Basilar Aneurysm and Bifurcation

J. Ortega*, J. Hartman†, J. Rodriguez‡, D. Maitland§

January 10, 2008

Corresponding author: Jason Ortega, Lawrence Livermore National Laboratory, P.O. Box 808, L-644, Livermore, CA 94551; e-mail: ortega17@llnl.gov; phone: 925-423-3824

*Staff Scientist, Engineering, Lawrence Livermore National Laboratory, Livermore, CA.
†Interventional Neuroradiologist, Department of Neurosurgery, Kaiser Permanente Medical Center, Sacramento, CA.
‡Post-College Appointee, Physics and Advanced Technologies, Lawrence Livermore National Laboratory, Livermore, CA.
§Associate Professor, Biomedical Engineering Department, Texas A&M University, College Station, TX.

Abstract

Aneurysm re-growth and rupture can sometimes unexpectedly occur following treatment procedures that were initially considered to be successful at the time of treatment and post-operative angiography. In some cases, this can be attributed to surgical clip slippage or endovascular coil compaction. However, there are other cases in which the treatment devices function properly. In these instances, the subsequent complications are due to other factors, perhaps one of which is the post-treatment hemodynamic stress. To investigate whether or not a treatment procedure can subject the parent artery to harmful hemodynamic stresses, computational fluid dynamics simulations are performed on a patient-specific basilar aneurysm and bifurcation before and after a virtual endovascular treatment. The simulations demonstrate that the treatment procedure produces a substantial increase in the wall shear stress. Analysis of the post-treatment flow field indicates that the increase in wall shear stress is due to the impingement of the basilar artery flow upon the aneurysm filling material and to the close proximity of a vortex tube to the artery wall. Calculation of the time-averaged wall shear stress shows that there is a region of the artery exposed to a level of wall shear stress that can cause severe damage to endothelial cells. The results of this study demonstrate that it is possible for a treatment procedure, which successfully excludes the aneurysm from the vascular system and leaves no aneurysm neck remnant, to elevate the hemodynamic stresses to levels that are injurious to the immediately adjacent vessel wall.

Keywords: aneurysm, computational fluid dynamics, post-treatment hemodynamic stresses

Abbreviations: CFD, computational fluid dynamics; SAH, subarachnoid hemorrhage

1 Introduction

Patients diagnosed with an aneurysm receive treatment by means of either endovascular coiling or surgical clipping. Despite their widespread use, these two treatment techniques are not always successful in eliminating the risk for subsequent aneurysm rupture and subarachnoid hemorrhage (SAH). For the coiling technique, one of the primary failure mechanisms leading to aneurysm re-growth, re-canalization, and re-bleeding is coil compaction [9, 10, 40, 48, 65, 67]. A dense packing of coils is necessary to promote blood stasis and subsequent isolation of the aneurysm from the vascular system. Yet, even in the best cases, the coiling material accounts for less than 50% of the total treated aneurysm volume [41, 46]. Consequently, coil compaction can occur and is especially problematic for giant aneurysms, large aneurysms containing thrombus, and aneurysms that project along the direction of blood flow in the parent artery [39, 88]. In addition, a loose packing of coils can lead to coil unraveling and migration into the parent artery and subsequent aneurysm re-growth [60, 88]. As a result, about 14% of the cases that are considered "successfully" treated at the time of coiling unexpectedly exhibit aneurysm recurrence [9]. Overall, the hemorrhage or re-hemorrhage rate after aneurysm coiling is roughly estimated to be 0.79% per patient-year [48], although this may be higher for incompletely treated aneurysms. For surgical clipping, the risk of re-growth for a completely clipped aneurysm is about 0.26-0.52% annually, while that for *de novo* aneurysm formation is about 0.89-1.8% [12, 79]. To reduce the number of these failed clipping procedures, clinicians have narrowed the definition of what constitutes an acceptable residual aneurysm neck during intraoperative angiography; 1-2 mm residual necks, which were once considered to be insignificant, are now eliminated when surgically feasible by placing the clip as flush as possible with the long axis of the aneurysm neck [55]. Despite these measures, aneurysm remnants, *de novo* aneurysms, re-growth, and rupture sometimes unexpectedly occur following procedures that were initially considered to be successful due to a perfect clip placement at the time of surgery and post-operative angiography [78]. In some cases, the treatment failure can be attributed to clip slippage or to a faulty clip [22]; however, there are other cases in which the clip functioned properly and complete aneurysm obliteration was achieved [7, 87].

While these latter types of failure may be due, in part, to the pathological factors, such as congenital defects, hypertension, atherosclerosis, and thrombosis, hemodynamics may also play an important role in the post-treatment pathogenesis of aneurysms [69, 87]. It is well documented in the literature that extreme hemodynamic stresses can have a detrimental effect upon the integrity of arteries [3, 13, 14, 15, 29, 30, 31, 32, 45, 53, 57, 81, 82]. Fry demonstrated that exposure of the artery wall to shear stresses of 37.9 Pa results in a significant deterioration of the endothelial surface [29]. The computational work of Hassen, *et al.* found a correlation between the aneurysm rupture locations and regions of high wall shear stress (WSS) [35]. In regions where the WSS is low and the wall shear stress gradient (WSSG) is high, such as that at points of flow separation and reattachment, the endothelial cells have high cell division rates and a low cell density, which can lead to the influx of low density lipoproteins and subsequent changes to the structural integrity

of the artery wall [86]. *In vitro* studies have also shown that endothelial cell function and growth are altered for wall shear stress gradients greater than 800 dynes/cm^3 [14, 15]. And, flow unsteadiness, which causes arterial wall vibrations or resonance, can have a degenerative effect on arterial wall properties [6, 26, 66]. If a treatment procedure either produces or does not eliminate hemodynamic stresses that are harmful to the artery walls, it would not be too surprising that arterial wall damage and subsequent SAH could occur following what was originally deemed a successful treatment. Consequently, a better understanding of post-treatment hemodynamic flow patterns and stresses within the vicinity of a treated aneurysm may not only highlight some of the possible mechanisms leading to these failed treatments, but may also guide medical device manufacturers in designing novel treatment techniques that could potentially reduce the risk for recurring SAH.

To help provide this understanding, we investigate the pre- and post-treatment hemodynamics of an aneurysm and parent artery using computational fluid dynamics (CFD) simulations. In particular, we investigate the following questions in this study. What types of flow patterns arise following the treatment of the aneurysm? How do these post-treatment flow patterns affect the hemodynamic stresses on the artery wall? And, is it possible for a successful aneurysm treatment to either produce or fail to eliminate potentially harmful hemodynamic stresses?

2 Setup

To address these questions, a virtual endovascular treatment is performed on the basilar aneurysm of a 44 year-old patient admitted to the Radiology Department at the U.C. Davis Medical Center. The aneurysm, which has a volume of 3.3×10^{-7} m^3 and neck area of 5.5×10^{-5} m^2, and the surrounding vascular arteries are obtained from CT scan data (Figure 1a-b). CAD software (Maya 6.0) is used to "treat" the aneurysm by replacing the aneurysm neck with a post-treatment lumen that represents the surface of an aneurysm filling material. Thus, only the flow within the parent artery lumen is modeled following the treatment. Defining the specific shape of the aneurysm filling material exposed to the post-treatment blood flow is somewhat subjective. Even though the virtual treatment procedure completely fills the aneurysm and leaves no "dog ears" around the periphery of the aneurysm neck, any number of shapes at the aneurysm neck could have been selected, leading to slight variations in the curvature of the exposed surface of the aneurysm filling material or in the location of the intersection between the filling material and the artery wall. To ensure that the resulting post-treatment lumen shape is representative of that seen in a typical treatment, an interventional neuroradiologist (J. Hartman) subsequently inspected this geometry and deemed it to be a successful "endovascular treatment" of the basilar aneurysm. Due to the significant computational time needed to obtain grid-converged solutions, the pre- and post-treatment simulations are conducted only on this particular basilar bifurcation. (For example, the calculation of the transient solution on the finest, post-treatment grid required 36 days of computing time on 128 2.4 GHz AMD Opteron CPUs. This translated

to 61 days when the waiting times in the batch computing queuing system were taken into account.) In future studies, we will have the opportunity to apply the present analysis to additional post-treatment basilar bifurcations, thus allowing us to determine the probability of our present findings within a larger sample size.

To properly apply the CFD boundary conditions needed to model the pre- and post-treatment flow patterns and stresses, we loft circular, cylindrical extensions from the basilar artery (BA), the two posterior cerebral arteries (PCA), and the two superior cerebellar arteries (SCA), respectively. We also assume that the aneurysm and artery walls are rigid. Ferguson [26] compared the elasticity of aneurysms to that of major intrancranial arteries and observed that aneurysms are relatively indistensible, indicating a loss of elastin within their walls. The *in vitro* experiments of Steiger, *et al.* [77] on lateral, saccular aneurysms demonstrated that the flow within an aneurysm is much more sensitive to the pulsatile nature of the cardiac waveform than to the effects of vessel wall deformation. Additionally, others [24, 62, 92] showed that although wall elasticity slightly decreases the magnitude of the wall shear stress, the overall flow and stress patterns within the vessel remain unchanged. Thus, the assumption of rigid walls is adequate for these simulations.

A pulsatile velocity boundary condition is specified at the inlet to the basilar artery. Since *in vivo* velocity data is not available for this particular patient, we use the cardiac waveform of Kato, *et al.* [50], who measured the mean velocity within a basilar artery using a contrast-enhanced 2D cine phase MR angiographic technique. With this *in vivo* data (Figure 2a), we employ the Womersley solution method [34, 37, 89] to compute the pulsatile velocity profile, $U(r,t)$, that is applied to the inlet (Figure 1a), where r is the radial distance from the centerline of the inlet and t is time. A pulse frequency of $f = 1.17$ Hz (70 beats/minute) is chosen, yielding a Womersley number, $0.5 d_o \sqrt{2\pi f \rho / \mu_o}$, of 2.96, where $d_o = 3.97 \times 10^{-3}$ m is the diameter of the inlet circular cylinder to the basilar artery, $\mu_o = 0.0035$ Pa·s is the characteristic viscosity of blood, and $\rho = 1060$ kg/m^3 is the characteristic density of blood [34, 37, 89]. At systole, which is taken to be the phase (2^o) of the maximum of the mean velocity over the cardiac cycle, the mean velocity, U_o, is 0.496 m/s, while at diastole, which is likewise taken to be the phase (219^o) of the minimum of the mean velocity, the mean velocity is 0.187 m/s. Over the entire cardiac cycle, the time-averaged mean velocity, $\overline{U}_o$, is 0.289 m/s, which corresponds to a time-averaged basilar artery flowrate of 3.58×10^{-6} m^3/s (214.8 cc/min). The corresponding maximum, minimum, and mean Reynolds numbers, $Re = \rho U_o d_o / \mu_o$, are 596, 225, and 347, respectively.

The viscosity of blood within the computational domain is modeled using a generalized power law [2], which closely agrees with the Carreau model [8] for low to mid-range shear and is effectively Newtonian for mid-range to high shear rates. Consequently, we anticipate that the Womersley velocity profile, $U(r,t)$, which is computed for a Newtonian fluid with a constant viscosity μ_o, will require a finite entrance length in order to become fully developed within the non-Newtonian fluid. To properly model the flow within the pre- and post-treatment basilar bifurcations, the length of the inlet circular cylinder extension must be greater

than this entrance length, y_e, which, for a pulsatile flow, is defined to be the distance along the pipe where the difference between the centerline velocity and its fully developed value is less than one percent of it time-averaged fully developed value [38]:

$$\frac{u(\infty, r=0, t) - u(y_e, r=0, t)}{\frac{1}{T}\int_0^T u(\infty, r=0, t)dt} = 0.01 \tag{1}$$

where T is the period (6/7 s) of the cardiac cycle. Rather than use the entire computational domain of the basilar bifurcation and aneurysm to determine the necessary entrance length, an iterative exercise that would require an excessive amount of CPU time for these unsteady simulations, we utilize a domain comprised of a circular cylinder of diameter d_o and length, $l = 43d_o$. The Womersley velocity profile is prescribed at the inlet to the cylinder and a no-slip boundary condition along the cylinder wall. A zero gradient boundary condition is specified at the cylinder outlet, such that the variables at the outlet nodes are extrapolated from the values at the interior nodes. The unsteady Navier-Stokes equations [51] are solved within this computational domain for a non-Newtonian fluid with a generalized power law viscosity model for blood. The simulation is run for one cardiac cycle to eliminate the initial transients and the pulsatile entrance length is subsequently computed over the second cardiac cycle. The maximum pulsatile entrance length, which occurs at a phase of 318^o, is found to be $5.4d_o$. Subsequent refinement of the mesh and doubling of the pipe length results in negligible changes (0.3% and 0.5%, respectively) to the pulsatile entrance length. The fully developed, non-Newtonian velocity profile (Figure 2b) closely resembles the Newtonian velocity profile in the region of high shear near the cylinder wall, though in the region of low shear at the cylinder center, the non-Newtonian velocity profile is more plug-like in appearance. With the results of this exercise in mind, we specify the length of the inlet circular cylinder extension to be $6d_o$, thus allowing the pulsatile velocity profile to become fully developed before entering the basilar artery of the patient.

To complete the specification of the boundary conditions, fractional outlet flowrates must be assigned to the two PCAs and two SCAs. Amin-Hanjani, *et al.* [1] made *in vivo* flowrate measurements on fifty healthy patients and observed that 72±22 and 68±18 cc/min of the 190±40 cc/min basilar artery inflow exits through the left and right PCAs, respectively. Likewise, in a comparative study of patients with and without preeclampsia, Zeeman, *et al.* [91] measured the left and right PCA flowrates within the healthy patients to be nearly equal. However, in neither these studies, nor in those reviewed in the literature, is *in vivo* flowrate data found for the left and right SCAs. Thus, for the sake of this study, we assume that the exiting flow is equally divided between the left and rights sides of the basilar bifurcation. Furthermore, we assume that 38.5% (82.7 cc/min) of the basilar artery inflow exits through each of the PCAs, a value about equal to the PCA flowrate fraction measured by Amin-Hanjani, *et al.* and Enzmann, *et al.* [25], and, by conservation of mass, that 11.5% (24.7 cc/min) of the remaining basilar artery inflow exits through each of the SCAs. Lastly, we apply a zero gradient boundary at the PCA and SCA outlets, such that the variables

at the boundary nodes are extrapolated from the values of the interior nodes.

The velocity, pressure, and viscosity fields are computed within the pre- and post-treatment bifurcations using a finite-volume CFD code [75]. The spatial fluxes within the Navier-Stokes equations are discretized with a second-order monotone advection and reconstruction scheme (MARS) [75], while the temporal derivatives are discretized by blending a second-order Crank-Nicholson scheme with a first-order implicit scheme, which reduces the over- and under-shooting of computed variables commonly observed with higher order schemes. The resulting order of this blended scheme is 1.8. A time step of 4×10^{-5} s is chosen, resulting in a mean (both spatial and temporal) Courant number that is of order 1 over all of the cells within the computational domain. The finite volume equations are solved using an implicit predictor-corrector PISO method [42, 43, 44], which utilizes operator splitting to temporarily decouple the flow equations from one another allowing them to be solved sequentially with an algebraic multigrid (AMG) approach [68]. At each time step, the residuals are reduced by at least three orders of magnitude. The velocity, pressure, and viscosity fields are initialized by running a steady state simulation with an inlet velocity profile of $U(r, t = 0)$ for a few thousand iterations. The transient simulation is then initialized with this "steady state" solution and run for three cardiac cycles to eliminate the initial transients in the flow field. Data sampling is made over two additional cardiac cycles.

In order to ensure that the computed results are not dependent upon grid resolution, the simulations of the post-treatment bifurcation are repeated on four trimmed cell grids [75] having sizes of 1.1×10^5 (G1), 4.0×10^5 (G2), 2.0×10^6 (G3), and 4.0×10^6 (G4) cells. The spatial average of the WSS in the area immediately surrounding the treated aneurysm neck (Figure 3a-b) exhibits grid independence for the three finest grids, as do the time-averaged and standard deviation (Figure 3c-d) of WSS through a slice ($x = 0$) of the bifurcation. However, only the two largest grids adequately capture the unsteady WSS signal, while the two coarser grids damp out the higher frequency content (Figure 3e). For this reason, the subsequent simulations of the post-treatment bifurcation are performed on the grid, G3, and those of the pre-treatment bifurcation on a grid with a comparable spatial resolution.

3 Results

The most apparent change to occur to the bifurcation flow field as a result of the treatment procedure is the elimination of a confined jet that is produced by the basilar artery flow issuing through the pre-treatment aneurysm neck. This jet, which spans nearly the entire length of the aneurysm prior to treatment, impinges upon the aneurysm wall in a skewed fashion, forming a large recirculation zone on the posterior side of the aneurysm as the jet reverses direction and exits through the aneurysm neck (Figure 4a). Following the treatment procedure, however, the basilar artery flow impinges instead upon the base of the filling material and produces a much smaller recirculation zone and a concentrated region of high-speed swirling flow on the anterior side of the bifurcation (Figure 4b). A comprehensive understanding of these flow field changes can

be obtained by examining the straining, S_{ij}, and rotational, Ω_{ij}, components of the velocity gradient tensor, $u_{i,j}$, an approach which has proven to be quite successful in identifying the coherent structures present in highly complex, three-dimensional flows [5, 23, 63, 73], where $S_{ij} = (u_{i,j} + u_{j,i})/2$ and $\Omega_{ij} = (u_{i,j} - u_{j,i})/2$ are the symmetric and skew-symmetric portions, respectively, of $u_{i,j}$. The tensor quantities S_{ij} and Ω_{ij} are computed within the volume bounded by the dark-shaded area in Figure 3a, which for the pre-treatment bifurcation also encompasses the aneurysm, and are interpolated onto a three-dimensional Cartesian mesh with a spacing of $\Delta_x = \Delta_y = \Delta_z = 6 \times 10^{-5}$ m, thus providing a uniform distribution of points from which probability statistics may be obtained. The joint probability density plots of $S^*_{ij}S^*_{ji}$ and $-\Omega^*_{ij}\Omega^*_{ji}$ (Figure 4c-f) for the pre- and post-treatment bifurcations highlight the underlying flow structures by comparing the relative importance of the straining and rotational components of the velocity gradient tensor, where the plotted quantities $S^*_{ij}S^*_{ji}$ and $-\Omega^*_{ij}\Omega^*_{ji}$ are the values of $S_{ij}S_{ji}$ and $-\Omega_{ij}\Omega_{ji}$ non-dimensionalized by $(\overline{U}_o/d_o)^2$. Points near the $S^*_{ij}S^*_{ji}$-axis are characterized by straining motion, while those near the $-\Omega^*_{ij}\Omega^*_{ji}$-axis by solid-body rotation; those points lying along the line $S^*_{ij}S^*_{ji} = -\Omega^*_{ij}\Omega^*_{ji}$ have nearly equal straining and rotational motions [5]. At both diastole and systole, the majority of the fluid within the pre- and post-treatment bifurcations exhibits nearly equal straining and rotational motions, indicating a predominantly "sheet-like" or shearing flow [73]. Though at diastole, it is evident that the treatment procedure increases the probability of both pure straining and pure rotational motions. At systole, there is a slight decrease in the amount of pure straining motion and a slight increase in the amount of rotational motion.

The flow structures corresponding to these probability distributions are visualized by plotting iso-surfaces of the second invariant of the velocity gradient tensor, $Q^* = \frac{1}{2}(-\Omega^*_{ij}\Omega^*_{ji} - S^*_{ij}S^*_{ji})$, which is equivalent to a 45 degree line with a $y-$intercept of $-2Q^*$ in Figure 4c-f. Clearly it follows that where Q^* is large and positive, the flow field is rotationally dominant ($-\Omega^*_{ij}\Omega^*_{ji} >> S^*_{ij}S^*_{ji}$); where Q^* is large and negative, it is straining dominant ($-\Omega^*_{ij}\Omega^*_{ji} << S^*_{ij}S^*_{ji}$); and where $Q^* = 0$, rotation and strain are equal to one another ($-\Omega^*_{ij}\Omega^*_{ji} = S^*_{ij}S^*_{ji}$). The iso-surfaces of $Q^* = 40$ indicate the presence of vortex tubes in the bifurcation. Prior to treatment, the aneurysm at systole is filled with a periodic train of these tubes (Figure 4g), which form at the aneurysm neck and advect upwards into the dome. However, the treatment procedure prevents the upward motion of these vortices, thus confining them along the junction of the aneurysm filling material and the artery wall. An example of this is plainly evident on the anterior side of the bifurcation (Figure 4h), in which a vortex tube, corresponding to the swirling flow region in Figure 4b, spans the entire bifurcation and extends downstream into the left PCA. Iso-surfaces of $Q^* = -40$ (not shown) at systole reveal that regions of the large straining motion arise at the stagnation zones of the basilar artery flow upon either the aneurysm wall (pre-treatment) or the filling material (post-treatment). Upstream of the bifurcation, no iso-surfaces of $Q = \pm 40$ are present. This is expected since the basilar artery flow in this region does not significantly deviate from the inlet Womersley velocity profile, which is characterized in general by a shearing motion with nearly equivalent magnitudes of fluid strain and rotation.

The confinement of the vortex tubes (Figure 5a-b) and the impingement of the basilar artery flow upon the aneurysm filling material establish distinct velocity fields that persist throughout the entire cardiac cycle. Profiles through the anterior vortex tube (along the z' axis in Figure 5b) of the vertical velocity component (Figure 5c) reveal a large downward velocity induced by the vortex. At systole, this profile exhibits a steep velocity gradient ($\approx 11,000$ s^{-1}) at the wall. On the posterior side of the basilar artery flow stagnation point ($d \approx 10.3 \times 10^{-3}$ m; see also Figure 4b), the horizontal velocity profiles (along the y' axis) indicate the presence of a wall jet (Figure 5d) with boundary layer thicknesses about equal to 0.25×10^{-3} m at diastole and 0.15×10^{-3} m at systole. At systole, the accompanying velocity gradient at the wall is likewise about $11,000$ s^{-1}. Large shear rates, such as these, exist throughout the post-treatment bifurcation, resulting in WSSs that are much greater than those present on the pre-treatment aneurysm wall. Prior to treatment, the WSS over aneurysm wall exhibits two distinct local maxima along the $x = 0$ cross-section (Figure 5e). The first ($d \approx 14 \times 10^{-3}$ at diastole; $d \approx 16 \times 10^{-3}$ m at systole) is due to the skewed impingement of the confined jet, while the second ($d \approx 24 \times 10^{-3}$ m at diastole and systole) occurs when the recirculating flow glances upon a convex protuberance of the aneurysm. By removing the cavity previously formed by the aneurysm, the treatment procedure forces the basilar artery flow to impinge in a nearly perpendicular manner upon the aneurysm filling material and to change direction over a much smaller volume, which, in turn, produces larger WSSs at diastole and especially at systole (Figure 5f). The local maximum in the post-treatment WSS at $d \approx 6 \times 10^{-3}$ m is caused by the adjacent vortex tube on the anterior side of the bifurcation. A qualitatively similar local increase in the WSS was shown by Walker [84] for a vortex placed in close proximity to a wall. On the other hand, the pair of maxima at $d \approx 8 \times 10^{-3}$ m and 10×10^{-3} m are due to the stagnation of the basilar artery flow upon the aneurysm filling material. The appearance of this pair of closely spaced peaks in WSS separated by a distinct local minimum ($d \approx 9 \times 10^{-3}$ m) is similar to the WSS distribution resulting from the impingement of an axisymmetric jet upon a plane [18, 19, 64]. (Note that the minimum in WSS at $d \approx 9 \times 10^{-3}$ m does not equal zero since the $x = 0$ cross section shown in Figure 5f does not coincide with the stagnation point at diastole and systole.) At systole, a secondary impingement ($d \approx 15 \times 10^{-3}$ m, see also Figure 4b) of the basilar artery flow also generates two closely spaced local maxima in WSS separated by a distinct local minimum, though the peak values of WSS are significantly less than those of the primary impingement.

In addition to altering the spatial distribution of WSS, the treatment procedure also affects its transient evolution. Prior to treatment, the most apparent temporal features in the WSS are those from the confined jet impingement and the recirculating flow that glances upon the convex protuberance (Figure 6a). These signatures are marked by a considerable amount of unsteadiness, which is evident by the periodically spaced, angled streaks at the beginning and latter phases of the cardiac cycle. The streaks are caused by the passage of the vortex tubes, whose transient presence is the result of a shear layer instability that develops on the confined jet (Figure 7a). The nominal vortex shedding frequency, which can be found from the phase spacing

of the streaks in Figure 6a, is about 70 Hz from $0^o <$ phase $< 40^o$. From the nominal slope of these WSS streaks, the convective velocity, U_c of the train of vortex tubes is found to be about 1×10^{-3} m/deg, or equivalently 0.4 m/s. Since the recirculating flow rotates clockwise within the aneurysm (when viewed from the left side of the patient), the streaks are sloped in one direction. The nominal wavelength, $\lambda = U_c/f$, of the shear layer instability is 6×10^{-3} m, a value that is on the order of that observed in the vorticity field at systole (Figure 7a). Following the treatment procedure, the WSS streaks are still evident on the bifurcation wall, though they do not persist to the extent seen prior to treatment (Figure 6b). This indicates that the removal of the aneurysm cavity suppresses the shear layer instability over portions of the cardiac cycle, which now has a more temporally uniform WSS distribution ($100^o <$ phase $< 300^o$) that is distinguished mainly by the signatures of the basilar artery flow impingement (7×10^{-3} m $< d < 11 \times 10^{-3}$ m) and the anterior vortex tube (5×10^{-3} m $< d < 6 \times 10^{-3}$ m). Over those phases in which the shear layer instability persists (Figure 7b), the frequency of the instability is increased slightly to about 90 Hz, as determined from the nominal phase spacing of the WSS streaks from $0^o <$ phase $< 40^o$.

The presence of high frequency, intra-aneurysmal flow unsteadiness is not unique to this particular patient, but has been observed in other aneurysms as well. Ferguson [26] and Ferguson & Roach [27] measured the *in vivo* flow oscillations of saccular aneurysms using a phonocatheter and found them to produce narrow-band sounds in the range of 300-600 Hz. It was deduced that these sounds, which in fact had a "musical quality" to them, were caused by turbulent flow within the aneurysm. In a recent computational study of a generic basilar aneurysm, Valencia, *et al.* [83] observed oscillatory WSSs on the aneurysm dome throughout the cardiac cycle. Even for a steady inlet boundary condition at the basilar artery, the WSS fluctuations had a dominant frequency of 17.5 Hz. Interestingly, when the aneurysm was removed from the vascular system and a healthy bifurcation modeled, Valencia, *et al.* showed a near complete elimination of the higher frequency WSS oscillations. Others [61, 70, 85] have observed similar frequencies within aneurysms using *ex vivo* "electronic stethoscopes." With an optical transducer, Simkins & Stehbens [72] recorded frequencies in the range of 10-30 Hz from measurements conducted on experimental saccular aneurysms. In much the same accord, Steiger & Reulen [76] observed frequencies in unsteady aneurysm flows in the range of 7-17 Hz from intra-operative Doppler recordings of patients undergoing a craniotomy. Steiger & Reulen also performed a study on rigid, glass models of generic aneurysms and confirmed the presence of flow oscillations in regions of the flow where deceleration occurred. One notable phenomenon they observed was for a terminal, saccular aneurysm. When a 50/50 branching ratio was imposed upon the two outlet arteries, the visualization dye was seen to fill the aneurysm in, what Steiger & Reulen referred to as, "irregular waves." Whether or not these "waves" are indications of a shear layer instability that rolls up into discrete vortex tubes is difficult to ascertain from the dye injection and streaming birefringence images presented in Fig. 4 of [77].

Across the entire surface of the post-treatment bifurcation, it is evident that the magnitude of WSS is dominated by the signatures of the confined vortex tube and the basilar artery flow impingement, unlike

the pre-treatment aneurysm in which the most distinct feature is an asymmetric annulus of raised WSS due to the impinging confined jet (Figure 7c-d). The WSS signature from the vortex tube has a quasi-2D appearance in the form of a narrow band that spans a region beneath the treated aneurysm. Near the center of this band ($x = 0$ m, $d = 5.7 \times 10^{-3}$ m), the magnitude of WSS varies over the cardiac cycle from a maximum of 51 Pa ($0.58\rho\overline{U}_o^2$) at phase = 1^o to a minimum of 8.7 Pa ($0.098\rho\overline{U}_o^2$) at phase of 230^o (Figure 8a). The WSS signature from the impinging basilar artery flow has a roughly axisymmetric distribution centered upon the flow stagnation point (Figures 7d and 8b), which is the location of a local minimum in the WSS. The transient location of this stagnation point is obtained by fitting the surrounding WSS data with a fifth-order polynomial surface and computing the location of the minimum value of WSS on this surface, thereby yielding sub-mesh resolution accuracy of the stagnation point at each cardiac phase. Over the course of the cardiac cycle, it is apparent that the stagnation point traverses a tortuous circuit that is fairly repeatable from one cycle to the next (Figure 8b). At both systole and diastole, plots of the WSS as a function of the radial distance, r_s, from the stagnation point demonstrate that the WSS increases from the stagnation point to a local maximum and then decreases at larger radial distances (Figure 8c-d). To determine, in general, how this maximum WSS and the radial location at which it occurs vary over the cardiac cycle, the WSS plots at each time step are fit in the vicinity ($0 \leq r_s \leq 1.75 \times 10^{-3}$ m) of the stagnation point with an empirical relationship,

$$\tau_w(r_s, t) = \frac{a_o(t)}{r_s}(1 - e^{-r_s^2/a_1(t)^2}) \tag{2}$$

that captures the overall features of the transient WSS distribution. It follows from Eq. 2 that the maximum WSS of the curve fit is

$$\tau_{w_{max}}(t) = 0.638\frac{a_0(t)}{a_1(t)} \tag{3}$$

and its radial location, $r_{s_{max}}$, is $1.12a_1(t)$ at each phase throughout the cardiac cycle. It is evident that $r_{s_{max}}$ remains within 1.3×10^{-3} m ($0.33d_o$) of the migrating stagnation point over the entire cardiac cycle (Figure 8e). Furthermore, $\tau_{w_{max}}$ varies from a minimum of 10 Pa ($0.11\rho\overline{U}_o^2$) at a phase of 230^o to a maximum value of 44 Pa ($0.50\rho\overline{U}_o^2$) at a phase of 8^o (Figure 8f) and displays a time-dependent behavior that is similar to that of the WSS due to the anterior vortex tube (see Figure 8a).

4 Discussion

In the major arteries throughout the human body, the nominal WSS ranges from about 0.2-2 Pa [16]. Near arterial branches and regions of sharp wall curvature, the WSS increases as shown in the simulations of Valencia *et al.* [83], in which the maximum WSS of non-Newtonian blood flow through a generic healthy

basilar bifurcation is on the order of 25 Pa. Yet, the present computational results demonstrate that across a signification portion of the aneurysm filling material and basilar artery wall, the treatment procedure produces WSSs that are several times greater than these nominal values. This could have an effect upon the post-treatment bifurcation, as a number of studies have shown that the WSS alters the properties of the endothelial cells lining the artery wall. For values of WSS less than approximately 0.5-1.5 Pa, the endothelial cells are randomly aligned and have a cobblestone, or polygonal shape [11, 13, 17, 49]. Endothelial cells with this shape occur not only in regions uniformly exposed to low WSS, but also in local low WSS regions in which there is flow separation or reattachment [14]. When the WSS is increased beyond 0.5-1.5 Pa, the cells elongate from a polygonal shape to an ellipsoidal shape and become uniformly oriented in the direction of the WSS [11, 13, 17]. While the response time for the endothelial cells to attain this ellipsoidal shape depends upon the magnitude of the applied WSS, it is typically on the order of several hours [17, 49]. The number of thick stress fibers that are parallel to the long axis of the cell increases after application of the WSS, thereby stiffening the cell [17, 49]. The cell height has also been observed to decrease by about 1-2 microns under the application of WSS [4, 74]. It has been suggested that the endothelial cells change their shape in this manner so as to minimize the total force on the cell nuclei [36]. Exposure of the endothelial cells to these nominal levels of WSS has a beneficial effect since the WSS tends to inhibit cell proliferation, which may prevent artherogenesis, and to upregulate various genes that are considered important in maintaining the integrity of the endothelial surface [20, 21, 28, 55, 80].

However, continued increases in the WSS can have a detrimental effect upon the integrity of the endothelial cells. For example, flow-induced trauma to the endothelium has been observed in several animal model studies, in which an artery is partially collapsed so as to increase the local WSS [32, 45, 53]. In some cases, the elevated WSS completely scours off the endothelial cells, thereby exposing the internal elastic lamina, or, in other cases, produces "cellular ulcers," consisting of cell membrane loss and of a thin layer of underlying cytoplasm [45]. To quantify the threshold values of WSS that result in damage to the endothelial cells, Fry conducted an animal model study in which a plug with a longitudinal groove was placed inside an animal aorta [29, 30]. The groove, which was adjacent to the endothelial surface, accelerated the blood flow, thereby generating a range of elevated WSSs. From these studies, Fry quantified two key values of the WSS: the acute critical yield stress, τ_{wc}, and the erosion stress, τ_{we}. The acute critical yield stress, measured to be 37.9 ± 8.5 Pa in [29] and 42.0 Pa in [30], is defined to be the time-averaged shear stress that results in the greatest rate of change of normal to abnormal endothelial cell forms through processes that Fry describes as "yielding," "melting," "dissolving," or "changing chemically," all of which lead to a distinct deterioration of the endothelial surface. The erosion stress (95.0 Pa) is defined to be the time-averaged shear stress at which the greatest number of cells is eroded from the endothelium [30]. In both cases, Fry found that the elevated WSSs produced distinct structural changes to the endothelium that increased the arterial wall permeability to macromolecules, such as low density lipoprotein. Fry also noted that since a finite amount of time is

necessary for damage to occur to the endothelium, τ_{we} exhibits a functional dependence upon the exposure time to elevated WSSs; for brief exposures, τ_{we} is large, while, for long exposures, τ_{we} gradually approaches τ_{wc}. In a later *in vitro* study, Vaishnav, *et al.* measured τ_{we} by impinging jets of physiological saline onto endothelium segments and by correlating the regions of cellular damage with the local WSSs for exposure times ranging from 30-7200 s [82]. After 30 s of exposure, τ_{we} was measured to be 505 Pa. However, an empirical curve fit of τ_{we} as a function time indicated that, for large exposure times, τ_{we} asymptotically approaches 60 Pa, a value comparable to the acute critical yield stress measured by Fry.

The treatment procedure of the basilar aneurysm produces a marked increase in the WSS to levels that are instantaneously greater than the acute critical yield stress (37.9 Pa). This is especially true at systole where the maximum WSS due to the vortex tube and the impinging basilar artery flow is approximately 50 Pa (see Figure 8a,c). At systole, the total area, A_c, exposed to a WSS greater than 37.9 Pa is 1.0×10^{-5} m^2, a surface area which is equal to 81% of the characteristic area, $A_o = \frac{\pi}{4} d_o^2$, of the inlet basilar artery (Figure 9a). Throughout the cardiac cycle ($0^o \leq$ phase $\leq 360^o$), A_c fluctuates from a maximum of 1.3×10^{-5} m^2 ($1.1 A_o$) at a phase of 4^o to a minimum of zero over phases 131^o to 288^o (Figure 9b). This is quite an increase in surface area when compared to the pre-treatment bifurcation, in which A_c is at most 1.8×10^{-6} m^2 ($0.14 A_o$) (over $0^o \leq$ phase $\leq 360^o$) at a phase of 13^o and is comprised of the regions where the confined jet impinges upon the aneurysm wall at $d \approx 15 \times 10^{-3}$ m and where the recirculating flow within the aneurysm glances upon the convex protuberance at $d \approx 24 \times 10^{-3}$ m (see Figure 5e). This increase in WSS also increases the fraction of time over the cardiac cycle in which the WSS exceeds the acute critical yield stress (Figure 9c). When time-averaged over the cardiac cycle, the WSS across the pre-treatment bifurcation remains less than 37.9 Pa. However for the post-treatment case, there is an area of 1.4×10^{-7} m^2 ($0.01 A_o$) at the junction of the right PCA and the basilar artery (Figure 9d) that is exposed to a time-averaged WSS greater than 37.9 Pa. Based upon the histological data of Fry, this area of the artery wall would subsequently undergo endothelial cytoplasmic swelling and cell deformation and disintegration. It should be noted that since the prescribed basilar artery flowrate in these simulations corresponds to a resting condition, the arterial wall area exposed to WSSs greater than the acute critical yield stress represents a lower bound of time-averaged damage. For exercise conditions, in which the basilar artery flowrate is elevated by an increase in both the cardiac frequency and the stroke volume of the heart, the magnitude of the time-averaged WSS would increase across the basilar bifurcation and, subsequently, enlarge the post-treatment area of endothelial cell damage.

The elevated WSSs could also lead to long-term arterial wall remodeling in the vicinity of the treated aneurysm neck. A number of studies [33, 47, 58, 71, 90, 93] have shown that arteries exposed to increased WSS remodel by expanding in diameter until the WSS returns to a nominal value. Masuda, *et al.* [58] observed that this expansion process arose from gaps in the internal elastic lamina. Over a period of several days, these gaps expanded to form circumferential depressions across the lumen surface. After several weeks,

the internal elastic lamina widened as the luminal depressions became interconnected with one another. Endothelial cells proliferated within these gaps, thereby providing a continuous cell lining over the expanded arterial lumen. By measuring artery diameters for vessels with and without endothelial cells, Langille & O'Donnell [52] showed that endothelial cells are necessary for this remodeling process to occur in response to changes in the WSS. Recently, Meng, *et al.* [59] observed two types of vessel remodeling within arterial bifurcations that were examined either 2 weeks or 2 months after their initial surgical generation. The first was an intimal pad that formed where the parent artery flow impinged upon the apex of the bifurcation. Within this region, the intima was thicker due to additional collagen and elastin layers. The second type of remodeling, located immediately adjacent to the intimal pad, differed in that it was injurious in nature and resulted in severe degradation of the arterial wall structure, including internal elastic lamina destruction and smooth muscle cell, fibronectin, and endothelial cell losses. Most notably, in five of the six bifurcations Meng, *et al.* investigated, a groove developed on the thinned media in this region, possibly indicating the early stages of aneurysm formation. The corresponding CFD simulations demonstrated that this region was exposed to substantially increased levels of WSS and the WSSG. Such remodeling could potentially occur over the post-treatment bifurcation in the present study. Perhaps, in the area adjacent to the vortex tube, the endothelial cells that survive outside the region of acute critical yield stress would lead to local vessel dilatation, which may reduce the velocity gradients, thus returning the WSS to nominal levels and ensuring the long-term success of the treatment procedure. On the other hand, the endothelial cell damage due to the extreme values of WSS could be so severe that the artery wall degrades in a manner similar to that of Meng, *et al.*, possibly resulting in aneurysm re-growth. Regardless, without *in vivo* data for this post-treatment geometry, it is difficult to determine at the present time exactly how vessel remodeling might proceed. In future animal model studies, we will be able to make direct correlations between the post-treatment hemodynamic stresses and the long-term outcome of treated aneurysms.

5 Conclusion

By performing a virtual endovascular procedure, we have investigated the post-treatment hemodynamics of a basilar aneurysm and bifurcation. The Womersley solution, computed from *in vivo* flowrate data, is specified at the inlet to the basilar artery, thereby supplying a physiological flow to the bifurcation. Prior to treatment, the velocity field within the aneurysm is comprised of a confined jet that is produced by the basilar artery flow issuing from the aneurysm neck. At systole, this jet undergoes an instability, in which the shear layers roll up into a periodic train of discrete vortex tubes. However, following the treatment procedure, in which the aneurysm is occluded, the basilar artery flow impinges instead upon the base of the aneurysm filling material, forming a stagnation zone and trapping a vortex tube along the anterior junction of the filling material and the basilar artery wall. The resulting WSS signatures produced by the flow stagnation and the vortex tube have magnitudes that are significantly greater than those present on

the pre-treatment artery and aneurysm walls. In fact, when time-averaged over the cardiac cycle, the WSS at the junction of the basilar artery and one of the PCAs has a magnitude that is greater than that shown by previous *in vivo* studies to cause severe damage to endothelial cells. Whether or not this increase in post-treatment hemodynamic stress is a common occurrence that leads to long-term aneurysm re-growth or rupture is beyond the scope of the present study and, therefore, remains to be determined in subsequent CFD simulations, animal model studies, and clinical investigations of additional patients. However, what is indicated by the present study is that the treatment procedure, while successful in occluding the aneurysm and leaving no neck remnant, elevates the WSSs to levels that are in theory injurious to the adjacent arterial wall.

The significant increase in WSS predicted by these simulations is a necessary consequence that results from occluding the aneurysm. Unfortunately, current endovascular treatment techniques do not offer the flexibility or fidelity to make small changes to the post-treatment lumen shape, which could possibly mitigate these extreme levels of WSS. However, there are other treatment techniques currently under development that may allow the WSSs to be tailored in the vicinity of the occluded aneurysm neck. An example of such a technique that could potentially be applied in this manner is one that utilizes a thermally-actuated shape memory polymer (SMP) foam that is delivered through a catheter to an aneurysm [56]. Since the shape into which the SMP foam is cut can be pre-determined, not only can patient-specific shapes be produced from pre-operation CT or MRI scans of the aneurysm, but optimized shapes that reduce the WSSs could also be machined into the SMP foam. One possible optimized shape for the present bifurcation could be one that gradually diverts the blood flow in the direction of the downstream arteries (Figure 10), potentially minimizing the extreme WSS signatures due to the vortex tubes and the impinging parent artery flow.

Acknowledgments

The authors would like to thank K. Salari for his guidance with the CFD simulations, J. Paschkewitz for his discussions on the probability statistics of the velocity gradient tensor, and W. Small for his feedback in the manuscript preparation. This work performed under the auspices of the U.S. Department of Energy by Lawrence Livermore National Laboratory under Contract DE-AC52-07NA27344. Major support provided by the National Institutes of Health/National Institute of Biomedical Imaging and Bioengineering, Grant R01EB000462. Additional support was provided by a LLNL Directed Research and Development Grant (04-ERD-093). UCRL-????????.

References

[1] Amin-Hanjani, S., X. Du, M. Zhao, K. Walsh, T.W. Malisch, and F.T. Charbel. Use of

quantitative magnetic resonance angiography to stratify stroke risk in symptomatic vertebrobasilar disease, *Stroke*, 1140-1145, http://stroke.ahajournals.org/cgi/content/full/36/6/1140, 2005.

[2] Ballyk, P.D., D.A. Steinman, and C.R. Ethier. Simulation of non-Newtonian blood flow in an end-to-end anastomosis, *Biorheology*, **31**(5):565-586, 1994.

[3] Bao, X., C. Lu, and J.A. Frangos. Temporal gradient in shear but not steady shear stress induces PDGF-A and MCP-1 expression in endothelial cells role of NO, NFκB, and *egr*-1, *Arterioscler. Thromb. Vasc. Biol.*, **19**:996-1003, 1999.

[4] Barbee, K. A., P. F. Davies, and R. Lal. Shear stress-induced reorganization of the surface topography of living endothelial cells imaged by atomic force microscopy, *Circ. Res.*, **74**:163-171, 1994.

[5] Blackburn, H.M., N.N. Mansour, and B.J. Cantwell. Topology of fine-scale motions in a turbulent channel, *JFM*, **310**:269-292, 1996.

[6] Bruns, D.L., J.E. Connolly, E. Holman, and R.C. Stofer. Experimental observations on poststenotic dilatation, *J. Thoracic Surg.*, **38**:662, 1959.

[7] Carlotti, C.G., Jr, N. Martelli, J.A. Assirati, Jr., H.R. Machado, A.C. Santos, and B.O. Colli. Subarachnoid hemorrhage after aneurysm surgery, *Arq Neuropsiquiatr*, **54**:181-189, 1996.

[8] Cho, Y.I. and K.R. Kensey. Effects of the non-Newtonian viscosity of blood on flows in a diseased arterial vessel. Part 1: Steady flows, *Biorheology*, **28**:241-262, 1991.

[9] Cognard C., A. Weill, L. Spelle, *et al.* Long-term angiographic follow-up of 169 intracranial berry aneurysms occluded with detachable coils, *Radiology*, **212**(2): 348-356, 1999.

[10] Conrad, M.D., I. Pelissou-Guyotat, C. Morel, G. Madarassy, C. Schonauer, and R. Deruty. Regrowth of residual ruptured aneurysms treated by Guglielmi's detachable coils which demanded further treatment by surgical clipping: report of 7 cases and review of the literature, *Acta Neurochir (Wien)*, **144**:419-426, 2002.

[11] Dardik, A., C. Leiling., J. Frattini, H. Asada, F. Aziz, F.A. Kudo, and B.E. Sumpio. Differential effects of orbital and laminar shear stress on endothelial cells, *J. Vasc. Surg.*, **41**(5):869-880, 2005.

[12] David, A.D., A.G. Vishten, R.F. Spetzler, M. Lemole, M.T. Lawton, and S. Partovi. Late angiographic follow-up review of surgically treated aneurysms, *J. Neurosurg.*, **91**:396-401, 1999.

[13] Davies, P.F., A. Remuzzi, E.J. Gordon, C.F. Dewey, and M.A. Gimbrone. Turbulent fluid shear-stress induces vascular endothelial-cell turnover *in vitro*, *Proc. Natl. Acad. Sci. U.S.A.*, **83**(7):2114-2117, 1986.

[14] DePaola, N., M.A. Gimbrone, Jr., P.F. Davies, and C.F. Dewey, Jr. Vascular endothelium responds to fluid shear stress gradients, *Arterioscler. Thromb.*, **12**(11), 1254-1257, 1992.

[15] DePaola, N., P.F. Davies, W.F. Pritchard, L. Florez, N. Harbeck, and D.C. Polacek. Spatial and temporal regulation of gap junction connexin43 in vascular endothelial cells exposed to controlled disturbed flows *in vitro*, *Proc. Natl. Acad. Sci. U.S.A.*, **96**:3154-3159, 1999.

[16] Dewey, C.F., Jr. Fluid mechanics of arterial flow, in *Dynamics of Arterial Flows*, Eds., Wolf, S. and N.T. Werthessen, *Advances in Experimental Medicine and Biology*, **115**, Plenum Press, 55-103, 1979.

[17] Dewey, C.F., Jr., S.R. Bussolari, M.A. Gimbrone, Jr., and P.F. Davies. The dynamic response of vascular endothelial cells to fluid shear stress, *J. Biomech. Eng.*, **103**:177-185, 1981.

[18] Deshpande, M.D. and R.N. Vaishnav. Submerged laminar jet impingement of a plane, *JFM*, **114**:213-236, 1982.

[19] Deshpande, M.D. and R.N. Vaishnav. Wall stress-distribution due to jet impingement, *J. Eng. Mech. ASCE*, **109**(2):479-493, 1983.

[20] Diamond S.L., J.B. Sharefkin, C. Dieffenbach, K. Fraisier-Scott, L.V. McIntire, and S.G. Eskin. Tissue plasminogen activator, messenger RNA levels increased in cultured human endothelial cells exposed to laminar shear stress, *J. Cell Physiol.*, **143**:364-371, 1990.

[21] Dimmeler S., C. Hermann, J. Galle, and A.M. Zeiher. Upregulation of superoxide dismutase and nitric oxide synthase mediates the apoptosis-suppressive effects of shear stress on endothelial cells, *Arterioscler. Thromb. Vasc. Biol.*, **19**:656-664, 1999.

[22] Drake, C.G., A.H. Friedman., and S.J. Peerless. Failed aneurysm surgery: reoperation in 115 cases, *J. Neurosurg*, **61**:848-856, 1984.

[23] Dubief, Y. and F. Delcayre. On coherent-vortex identification in turbulence, *Journal of Turbulence*, **1**:1-22, 2000.

[24] Duncan, D.D., *et al.* The effect of compliance on wall shear in casts of a human aortic bifurcation, *J. Biomech. Eng.*, **112**:183-188, 1990.

[25] Enzmann D.R., M.R. Ross, M.P. Marks, and N.J. Pelc. Blood flow in major cerebral arteries measured by phase-contrast cine MR, *AJNR*, **15**(1):123-9, 1994.

[26] Ferguson, G.G. Turbulence in human intracranial saccular aneurysms, *J. Neurosurg.*, **33**:485-497, 1970.

[27] Ferguson, G.G. and M.R. Roach. Flow Conditions at Bifurcations as Determined in Glass Models, with Reference to the Focal Distribution of Vascular Lesions, in Bergel, V.H. and H. Derek, *Cardiovascular Fluid Dynamics*, **2**:141-156, Academic Press, London, 1972.

[28] Frangos J.A., S.G. Eskin, L.V. McIntire, and C.L. Ives.. Flow effects on prostacyclin production by cultured human endothelial cells, *Science*, **227**:1477-1479, 1985.

[29] Fry, D.L. Acute vascular endothelial changes associated with increased blood velocity gradients, *Circ. Res.*, **22**(2):165-97, 1968.

[30] Fry, D.L. Certain histological and chemical responses of the vascular interface to acutely induced mechanical stress in the aorta of the dog, *Circ. Res.*, **24**:93-108, 1969.

[31] Fry D.L. Responses of the arterial wall to certain physical factors, In: *Atherogenesis: Initiating Factors*, Amsterdam: Ciba Found. Symp., 93-125, 1973.

[32] Gertz, S.D., *et al.* Endothelial cell damage and thrombus formation after partial arterial constriction: relevance to the role of coronary artery spasm in the pathogenesis of myocardial infarction, *Circulation*, **63**(3), 1981.

[33] Girerd, X., G. London, P. Boutouyrie, J.J. Mourad, M. Safar, and S. Laurent. Remodeling of the radial artery in response to a chronic increase in shear stress, *Hypertension*, **27**:799-803, 1996.

[34] Hale, J.F., D.A. McDonald, and J.R. Womersely. Velocity profiles of oscillating arterial flow, with some calculations of viscous drag and the Reynolds number, *J. Physiol.*, **128**:629-640, 1955.

[35] Hassan, T., E.V. Timofeev, T. Saito, H. Shimizu, M. Ezura, T. Tominaga, A. Takahashi, and K. Takayama. Computational replicas: anatomic reconstructions of cerebral vessels as volume numerical grids at three-dimensional angiography, *AJNR*, **25**:1356-1365, 2004.

[36] Hazel A.L. and T.J. Pedley Vascular endothelial cells minimize the total force on their nuclei, *Biophysical Journal*, **78**(1):47-54 , 2000.

[37] He, X., D.N. Ku, and J.E. Moore, Jr. Simple calculation of the velocity profiles for pulsatile flow in a blood vessel using Mathematica, *Ann. Biomed. Eng.*, **21**:45-49, 1993.

[38] He, X. and D.N. Ku. Unsteady entrance flow development in a straight tube, *J. Biomech. Eng.*, **116**:355-360, 1994.

[39] Hoh, B.L., J.D. Rabinov, J.C. Pryor, and C.S. Ogilvy. A modified technique for using elastase to create saccular aneurysms in animals that histologically and hemodynamically resemble aneurysms in human, *Acta Neurochir (Wien)*, **146**:705-711, 2004.

[40] Hope, J.K.A., J.V. Byrne, and A.J. Molyneux. Factors influencing successful angiographic occlusion of aneurysms treated by coil embolization, *AJNR*, **20**:391-399, 1999.

[41] Horowitz, M.D. Samson, and P. Purdy. Does electrothrombosis occur immediately after embolization of an aneurysm with Guglielmi detachable coils?, *AJNR*, **18**:510-513, 1997.

[42] Issa, R.I. Solution of the implicitly discretized fluid-flow equations by operator-splitting, *J. Comp. Phys.*, **62**(1):40-65, 1986.

[43] Issa, R.I., A.D. Gosman, and A.P. Watkins. The computation of compressible and incompressible recirculating flows by a non-Iterative implicit scheme, *J. Comp. Phys.*, **62**:66-82, 1986.

[44] Issa, R.I., B. Ahmadibefrui, K.R. Beshay, *et al.*, Solution of the implicitly discretized reacting flow equations by operator-splitting, *J. Comp. Phys.*, **93**(2):388-410, 1991.

[45] Joris I., T. Zand, and G. Majno. Hydrodynamic injury of the endothelium in acute aortic-stenosis, *American Journal of Pathology*, **106**(3):394-408, 1982.

[46] Kallmes, D.F., A.D. Williams, H.J. Cloft, M.B.S. Lopez, G.R. Hankins, and G.A. Helm. Platinum coil-mediated implantation of growth factor-secreting endovascular tissue grafts: an *in vivo* study, *Radiology*, **207**:519-523, 1998.

[47] Kamiya, A. and T. Togawa. Adaptive regulation of wall shear stress to flow change in the canine carotid artery, *Am. J. Physiol. Heart Circ. Physiol.*, **239**:H14-H21, 1980.

[48] Kang, H.-S., M.H. Han, B.J. Kwon, O.-K. Kwon, and S.H. Kim. Repeat endovascular treatment in postembolization recurrent intracranial aneurysms, *Neurosurgery*, **58**:60-70, 2006.

[49] Kataoka, N. and M. Sato. The change of F-actin distribution and morphology of cultured bovine aortic endothelial cells in the early stage of fluid shear stress exposure, *Trans. Jpn. Soc. Mech. Eng.*, **64**:1801-1808, 1998.

[50] Kato, T., T. Indo, E. Yoshida, *et al.* Contrast-enhanced 2D cine phase MR angiography for measurement of basilar artery blood flow in posterior circulation ischemia, *AJNR*, **23**:1346-1351, 2002.

[51] Kundu, P.K. *Fluid Mechanics*, Academic Press, 1990.

[52] Langille, B.L. and F. O'Donnell. Reductions in arterial diameter produced by chronic decreases in blood flow are endothelium-dependent, *Science*, **231**:405-407, 1986.

[53] Langille, B.L., MA. Reidy, and R.L. Kline. Injury and repair of endothelium at sites of flow disturbances near abdominal aortic coarctations in rabbits, *Arteriosclerosis*, **6**(2):146-154, 1986.

[54] Lendlein, A. and R. Langer. Biodegradable, elastic shape-memory polymers for potential biomedical applications, *Science*, **296**(5573):1673-6, 2002.

[55] Lin, T., A.J. Fox, and C.G. Drake. Regrowth of aneurysm sacs from residual neck following aneurysm clipping, *Journal of Neurosurgery*, **70**(4):556-560, 1989.

[56] Maitland, D.J., W. Small IV, J.M. Ortega, P.R. Buckley, J. Rodriguez, J. Hartman, and T.S. Wilson. Prototype laser-activated shape memory polymer foam device for embolic treatment of aneurysms, *J. Biomed. Opt.*, **12**(3):030504, 2007.

[57] Masuda H., Y. Kikuchi, T. Nemoto, A. Bukhari, T. Togawa, and A. Kamiya. Ultrastructural-changes in the endothelial surface of the canine carotid-artery induced by wall shear-stress load, *Biorheology*, **19**(1-2):197-208, 1982.

[58] Masuda, H., Y.-J. Zhuang, T.M. Singh, K. Kawamura, M. Murakami, C.K. Zarins, and S. Glagov. Adaptive remodeling of internal elastic lamina and endothelial lining during flow-induced arterial enlargement, *Arterioscler Thromb Vasc Biol.*, **19**:2298-2307, 1999.

[59] Meng, H., Z. Wang, Y. Hoi, L. Gao, E. Metaxa, D.D. Swartz, and J. Kolega. Complex hemodynamics at the apex of an arterial bifurcation induces vascular remodeling resembling cerebral aneurysm initiation, *Stroke*, **38**:1924-1931, 2007.

[60] Mori, K., Y. Nakao, N. Horinaka, R. Wada, A. Hirano, and M. Maeda. Cerebral aneurysm regrowth and coil unraveling after incomplete Guglielmi detachable coil embolization: serial angiographical and histological findings, *Neurol. Med. Chir. (Toyko)*, **43**:293-297, 2003.

[61] Olinger, C.P. and J.F. Wasserman. Electronic stethoscope for detection of cerebral aneurysm, vasospasm and arterial Disease, *Surg. Neurol.*, **8**:298-312, 1977.

[62] Perktold, K. and G. Rappitsch. Computer simulation of local blood flow and vessel mechanics in a compliant carotid artery bifurcation model, *J. Biomechanics*, **28**(7):845-856, 1995.

[63] Perry, A.E. and M.S. Chong. Topology of flow patterns in vortex motions and turbulence, *Applied Scientific Research*, **53**:357-374, 1994.

[64] Phares, D.J., G.T. Smedley, and R.C. Flagan. The wall shear stress produced by the normal impingement of a jet upon a flat surface, *JFM*, **418**:351-375, 2000.

[65] Reul, J., J. Weis, U. Spetzger, T. Konert, C. Fricke, and A. Thron. Long-term angiographic and histopathologic findings in experimental aneurysms of the carotid bifurcation embolized with platinum and tungsten coils, *AJNR*, **18**:35-42, 1997.

[66] Roach, M.R. Changes in arterial distensibility as a cause of poststenotic dilatation, *Am. J. Cardiol.*, **12**:802-15, 1963.

[67] Ross, I.B. and G.S. Dhillon. Complications of endovascular treatment of cerebral aneurysms, *Surgical Neurology*, **64**:12-19, 2005.

[68] Ruge, J.W. and K. Stüben. Algebraic Multigrid (AMG), in Multigrid Methods, Ed. S. McCormick, *Frontiers in Applied Mathematics*, SIAM, **5**, Philadelphia, 1986.

[69] Sahs, A.L. Observations on the pathology of saccular aneurysms, *J. Neurosurgery*, **24**(4):792-806, 1966.

[70] Sekhar, L.N. and J.F. Wasserman. Noninvasive detection of intracranial vascular lesions using an electronic stethoscope, *J. Neurosurg.*, **60**:553-559, 1984.

[71] Sho, E., *et al.* Arterial enlargement, tortuosity, and intimal thickening in response to sequential exposure to high and low wall shear stress, *J. Vasc. Surg.*, **39**:601-12, 2004.

[72] Simkins, T.E. and W.E. Stehbens. Vibrations recorded from the adventitial surface of aneurysms and arteriovenous fistulas, *Vasc. Surg.*, **8**:153-165, 1974.

[73] Soria J., R. Sondergaard, B.J. Cantwell, M.S. Chong, and A.E. Perry. A study of the fine-scale motions of incompressible time-developing mixing layers, *Phys. Fluids*, **6**(2):871-884, 1994.

[74] Stamatas, G.N. and L.V. McIntire. Rapid flow-induced responses in endothelial cells, *Biotechnology Progress*, **17**(3):383-402, 2001.

[75] STAR-CD, v3.24, v3.26, v4.0, CD-Adapco Group, *www.cd-adapco.com*.

[76] Steiger, H.J. and H.-J. Reulen. Low frequency flow fluctuations in saccular aneurysms, *Acta Neurochirurgica*, **83**:131-137, 1986.

[77] Steiger, H.J., A. Poll, D. Licpsch, and H.-J. Reulen. Haemodynamic stress in lateral saccular aneurysms, *Acta Neurochirurgica*, **86**:98-105, 1987.

[78] Thornton, J., Q. Bashir, V.A. Aletich, G.M. Debrun, J.I. Ausman, and F.T. Charbel. What percentage of surgically clipped intracranial aneurysms have residual necks?, *Neurosurgery*, **46**(6):1294-1300, 2000.

[79] Tsutsumi, K., K. Ueki, A. Morita, M. Usui, and T. Kirino. Risk of aneurysm recurrence in patients with clipped cerebral aneurysms: results of long-term follow-up angiography, *Stroke*, **32**:1191-1194, 2001.

[80] Urbich C., D.H. Walter, A. Zeiher, and S. Dimmeler. Laminar shear stress upregulates integrin expression. Role in endothelial cell adhesion and apoptosis, *Circ. Res.*, **87**:683-689, 2000.

[81] Vaishnav, R.N., H.B. Atabek, and D.J. Patel, Properties of intimal layer and adjacent flow, *J. Engng. Mech. Div. Proc. A.S.C.E.*, **104**:67-77, 1978.

[82] Vaishnav R.N., D.J. Patel, H.B. Atabek, M.D. Deshpande, F. Plowman, and J. Vossoughi. Determination of the local erosion stress of the canine endothelium using a jet impingement method, *J. Biomech. Eng.*, **105**(1):77-83, 1983.

[83] Valencia, A.A., A.M. Guzmán, E.A. Finol, and C.H. Amon. Blood flow dynamics in saccular aneurysm models of the basilar artery, *J. Biomech. Eng.*, **128**:516-526, 2006.

[84] Walker, J.D.A. The boundary layer due to a rectilinear vortex, *Proc. R. Soc. Lond. A*, **359**:167-188, 1978.

[85] Wasserman, J.F. *The Acoustic Detection of Cerebral Aneurysms*, Ph.D. Thesis, The University of Cincinnati, 1975.

[86] Weinbaum S. and S. Chien. Lipid transport aspects of atherogenesis, *J. Biomech. Eng.*, **115**(4B):602-10, 1993.

[87] Wermer, M.J., G.J. Rinkel, P. Greebe, K.W. Albrecht, C.M. Dirven, and C.A Tulleken. Late recurrence of subarachnoid hemorrhage after treatment for ruptured aneurysms: patient characteristics and outcomes, *Neurosurgery*, **56**(2):197-204, 2005.

[88] Willinsky, R.A. Detachable coils to treat intracranial aneurysms, *Canadian Medical Association Journal*, **161**(9):1136, 1999.

[89] Womersley, J.R. Method for the calculation of velocity, rate of flow and viscous drag in arteries when the pressure gradient is known, *J. Physiol.*, **127**:553-563, 1955.

[90] Zarins, C.K., M.A. Zatina, D.P. Giddens, D.N. Ku, and S. Glagov. Shear stress regulation of artery lumen diameter in experimental atherogenesis, *J. Vasc. Surg.*, **5**(3):413-420, 1987.

[91] Zeeman, G.G., M.R. Hatab, and D.M. Twickler. Increased cerebral blood flow in preeclampsia with magnetic resonance imaging, *American Journal of Obstetrics and Gynecology*, **191**:1425-9, 2004.

[92] Zhao, S.Z., *et al.* Blood flow and vessel mechanics in a physiologically realistic model of a human carotid arterial bifurcation, *Journal of Biomechanics*, **33**:975-984, 2000.

[93] Zhuang, Y.J., T.M. Singh, C.K. Zarins, and H. Masuda. Sequential increases and decreases in blood flow stimulate progressive intimal thickening, *Eur. J. Vasc .Endovasc. Surg.*, **16**:301-310, 1998.

Figure 1: Pre- and post-treatment geometries of the basilar aneurysm and bifurcation.

Figure 2: a) Mean velocity through a basilar artery as measured *in vivo* by Kato, *et al.* [50]. b) Velocity profiles for the Womersley solution (solid line), the present Newtonian CFD simulations ($\circ\ \circ\ \circ$), and a non-Newtonian, generalized power law fluid [2] (dashed line) for fully-developed, pulsatile flow in a circular pipe of diameter, $d_o = 3.97 \times 10^{-3}$ m.

Figure 3: a) Interrogation area for computing the spatial mean of the WSS across the bifurcation. b) Spatial average of the WSS across the interrogation area over two cardiac cycles, c) average and d) standard deviation of the WSS along $x = 0$ of the post-treatment bifurcation, and e) the fast Fourier transform of the unsteady, post-treatment WSS at $x = 0$, $d = 15 \times 10^{-3}$ m for four different mesh resolutions (G1, G2, G3, G4).

Figure 4: Velocity magnitude and streamlines at systole for the a) pre- and b) post-treatment bifurcations at $x = 0$. Joint probability density plots of $S^*_{ij}S^*_{ji}$ and $-\Omega^*_{ij}\Omega^*_{ji}$ for the c,e) pre- and d,f) post-treatment bifurcations at c,d) diastole and e,f) systole. Iso-surfaces of $Q^* = 40$ for the g) pre- and h) post-treatment bifurcations at systole.

Figure 5: Contours of $Q^* > 0$ at systole for the a) pre- and b) post-treatment bifurcations at $x = 0$. c) y- and d) z-components of the velocity field along the z'- and y'-axes (see Figure 5b), respectively, of the post-treatment bifurcation at systole. WSS at $x = 0$ for the e) pre- and f) post-treatment bifurcations at systole (solid line) and diastole (dashed line).

Figure 6: Spatial-temporal plot of the WSS at $x = 0$ for the a) pre- and b) post-treatment bifurcations.

Figure 7: Contours of the $x-$component of vorticity, ω_x, at $x = 0$ for the a) pre- and b) post-treatment bifurcations ($\omega_x < 0$, gray contours; $\omega_x > 0$, black contours), where $\omega = \nabla \times \mathbf{u}$. WSS across the c) pre- and d) post-treatment bifurcations at systole. The black arrows highlight the WSS signature of the impinging basilar artery flow. For the post-treatment bifurcation, the black arrow is directed at the basilar artery flow stagnation point, while the white arrow indicates the WSS signature due to the vortex tube that is adjacent to the artery wall.

Figure 8: a) Post-treatment WSS at $x = 0$, $d = 5.7 \times 10^{-3}$ m (see Figures 3 or 5 for the definition of d) due to the vortex tube adjacent to the artery wall. b) Transient location of the stagnation point arising from the impinging basilar artery flow upon the aneurysm filling material. The gray contours indicate the magnitude of the WSS surrounding the stagnation point at systole. Radial distribution of the post-treatment WSS in the vicinity of the basilar artery flow stagnation point at c) systole and d) diastole. The solid lines denote the WSS curve fit defined in Eq. 2. e) Radial location, $r_{s_{max}}$, of the f) maximum WSS, $\tau_{w_{max}}$, from the curve fit.

Figure 9: a) Contour of the area, A_c (black), in which the post-treatment WSS is greater than 37.9 Pa at systole. b) A_c as a function cardiac phase for the pre- (solid line) and post-treatment (dashed line) bifurcations. c) Fraction of time over two cardiac cycles in which the pre- and post-treatment WSS at $x = 0$ is greater than 37.9 Pa. d) Contour of the area, A_c (black), in which the time-averaged, post-treatment WSS is greater than 37.9 Pa.

Figure 10: Schematic of the SMP foam aneurysm treatment technique with a tapered geometry that gradually redirects the parent artery flow into the downstream arteries.

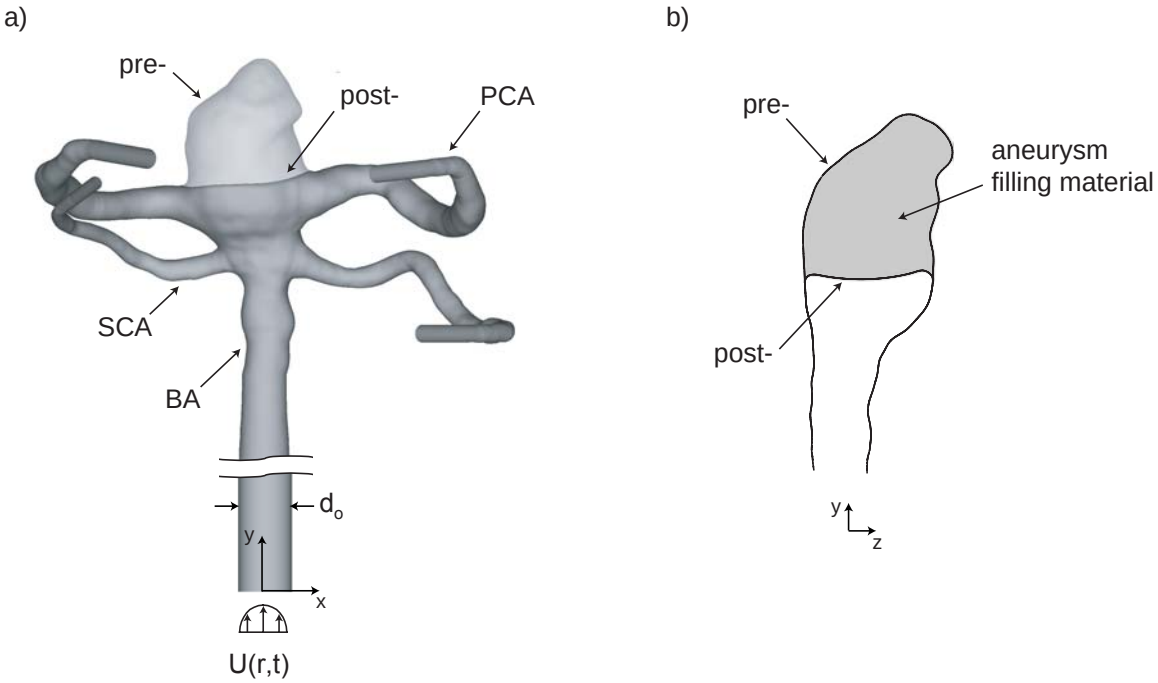

Figure 1. Ortega, *et al.*

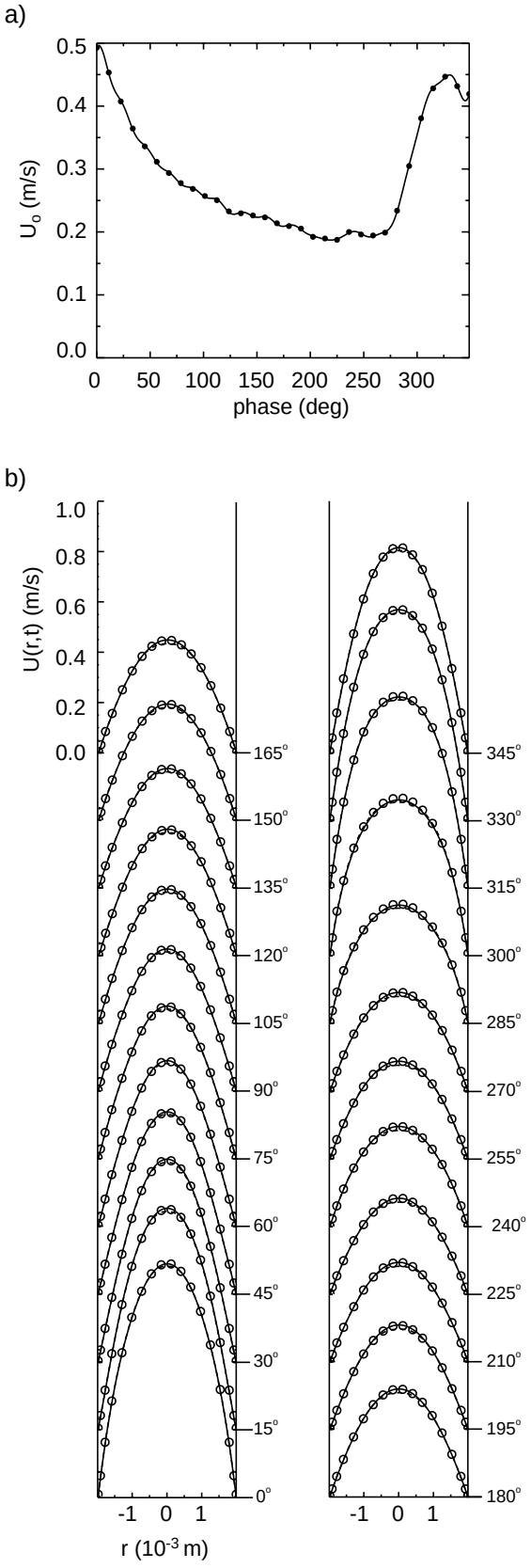

Figure 2. Ortega, *et al.*

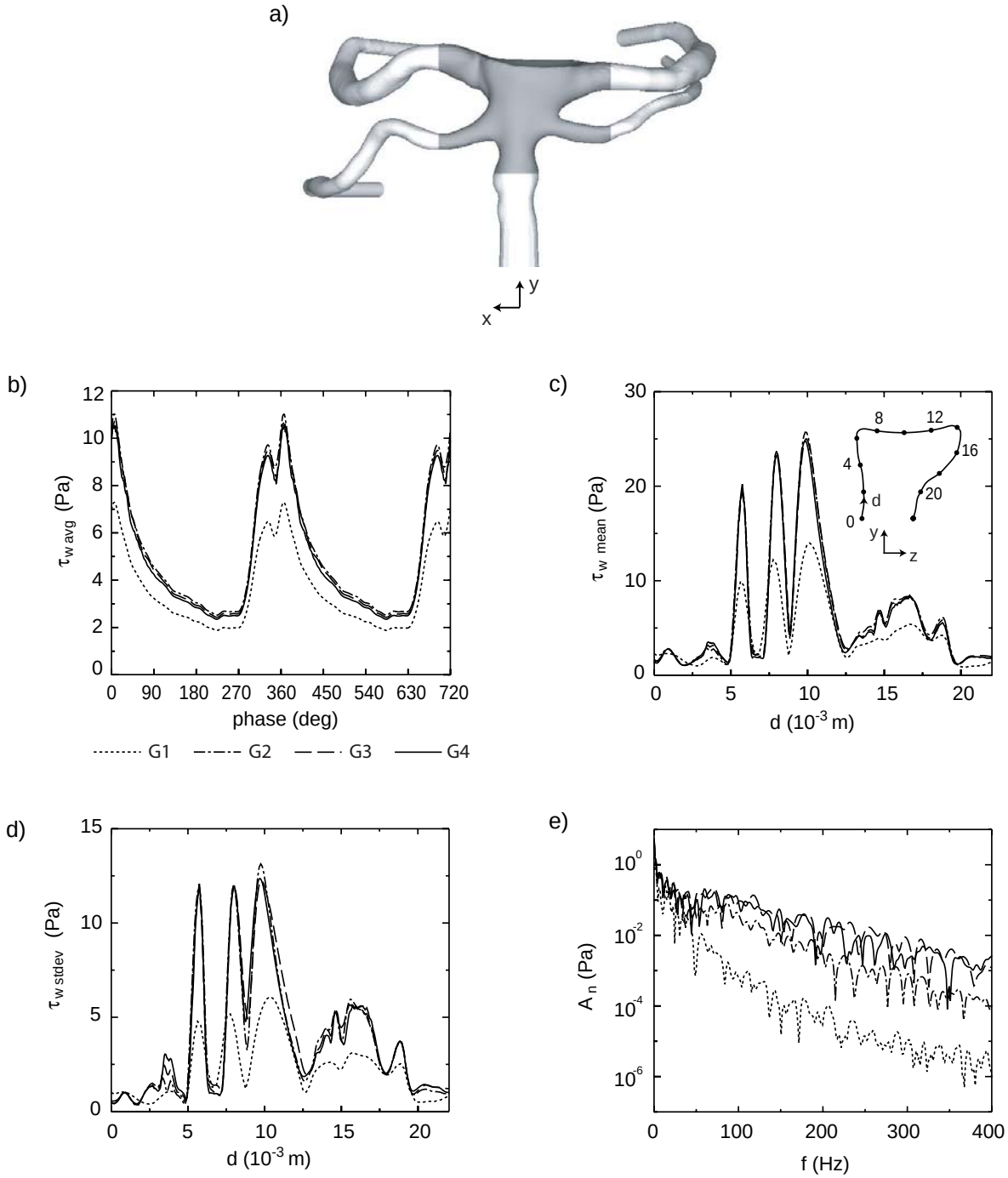

Figure 3. Ortega, *et al.*

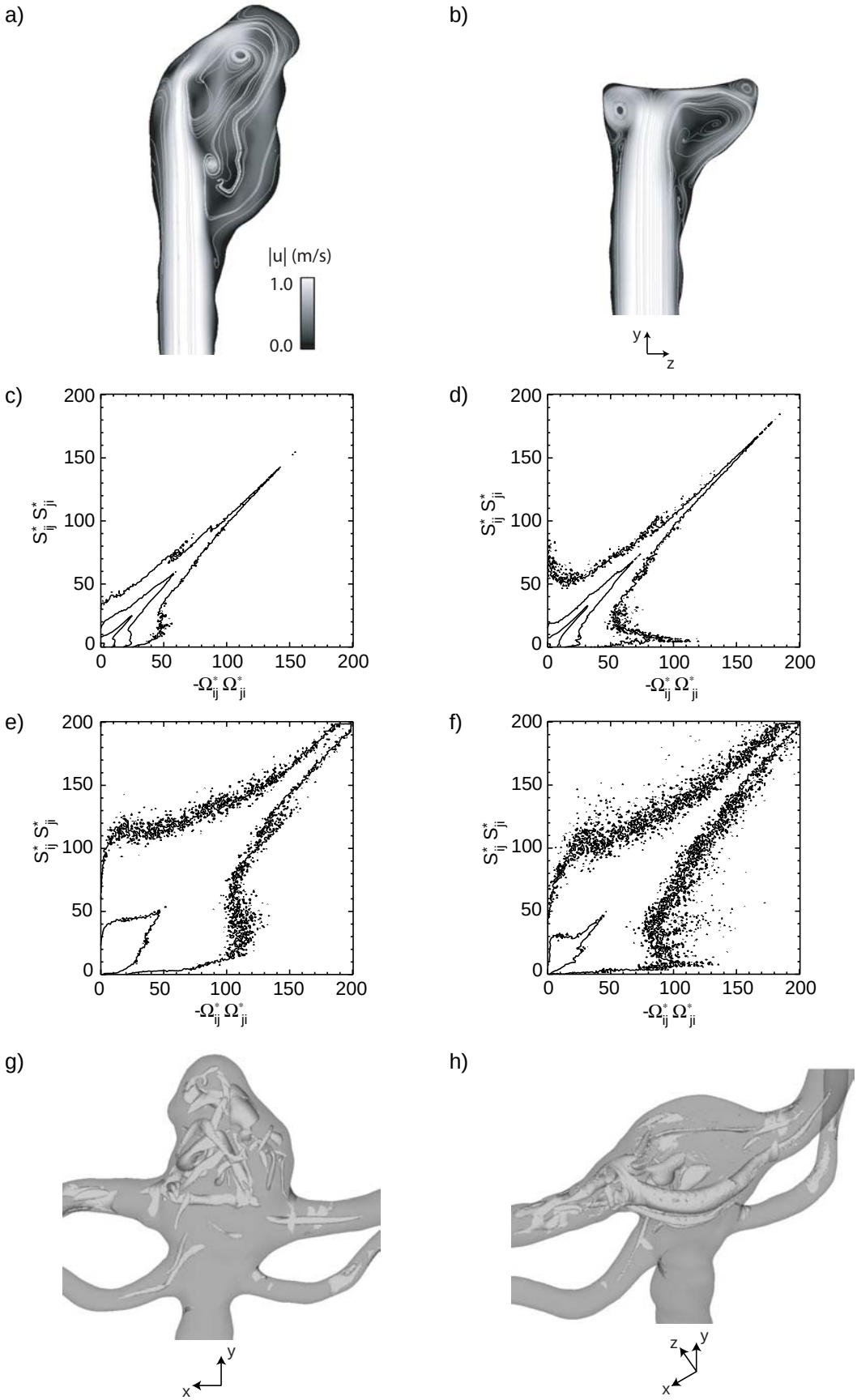

Figure 4. Ortega, *et al.*

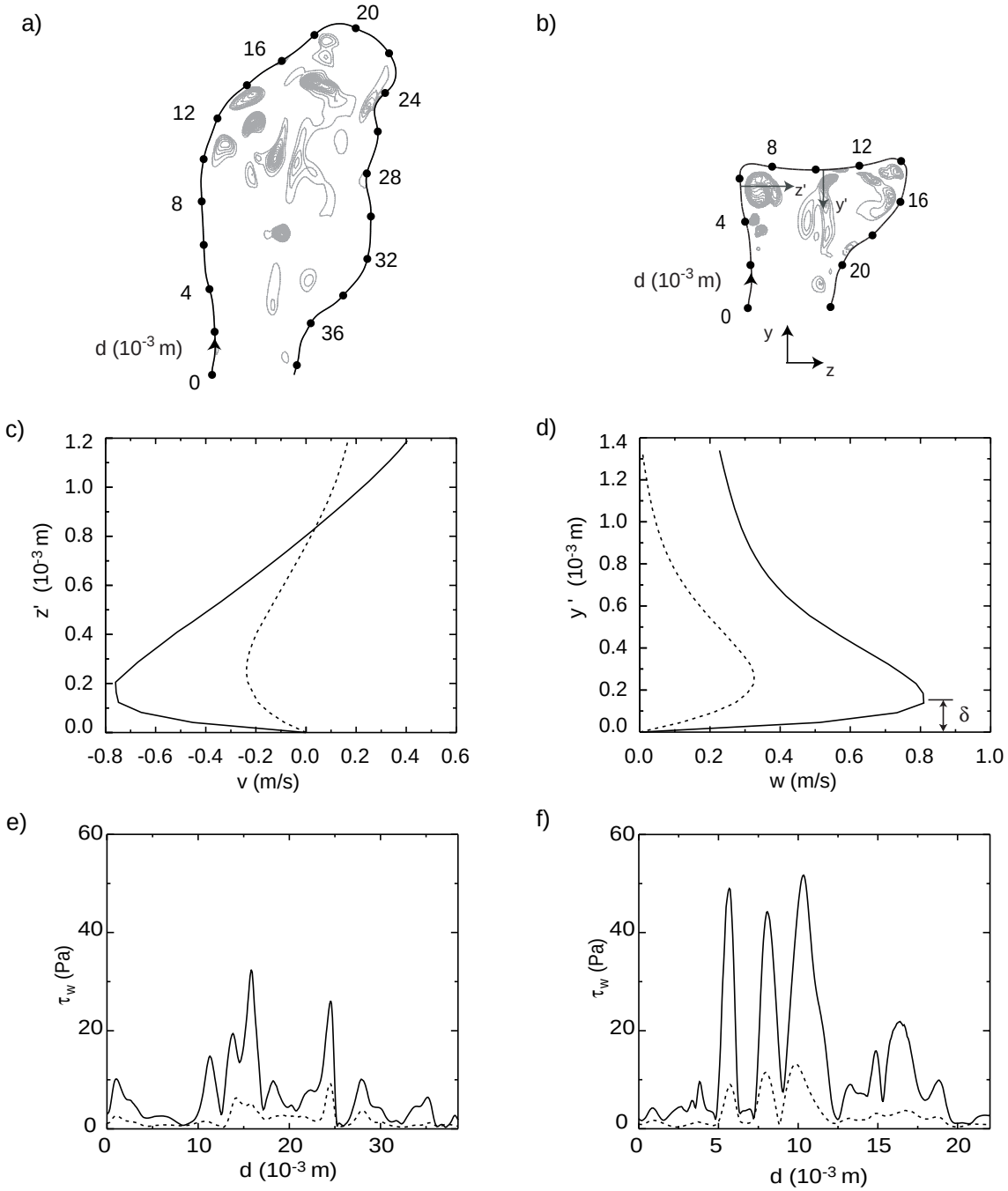

Figure 5. Ortega, *et al.*

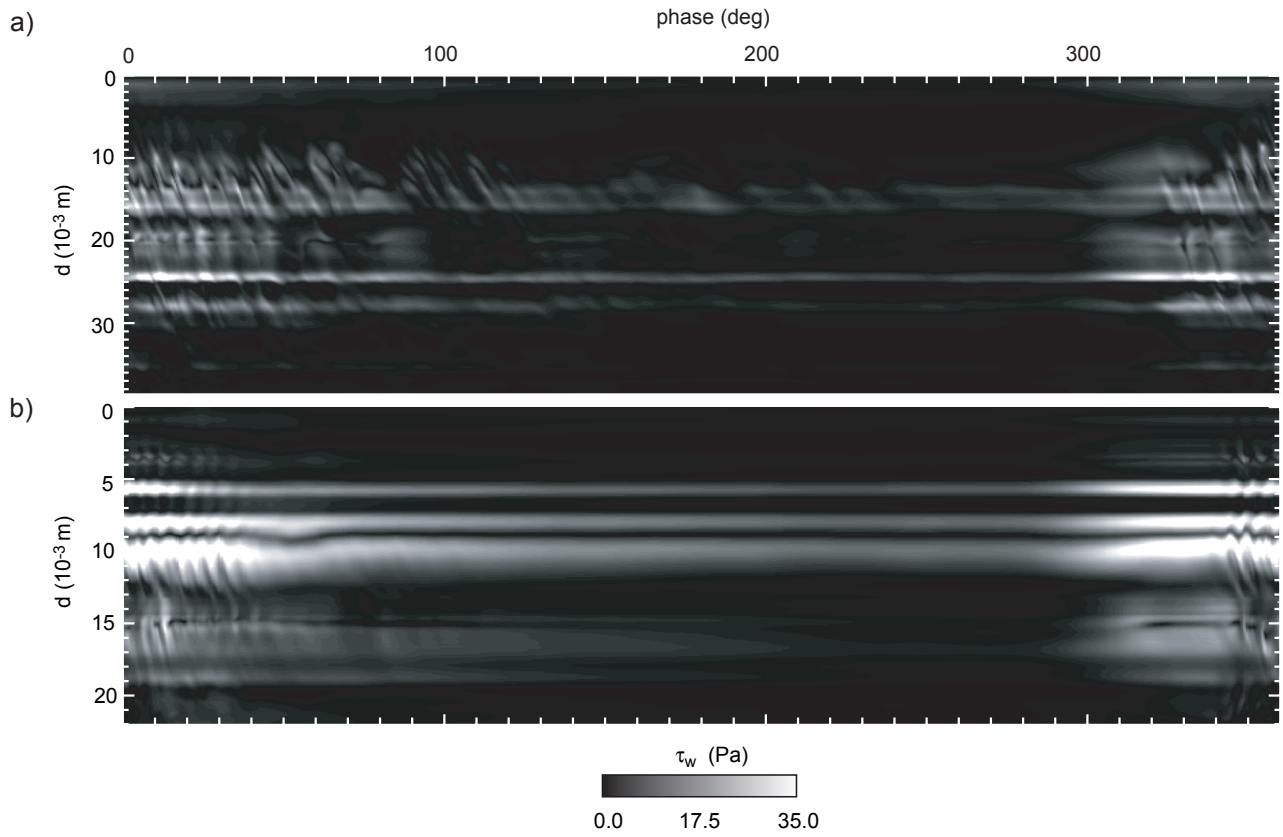

Figure 6. Ortega, *et al.*

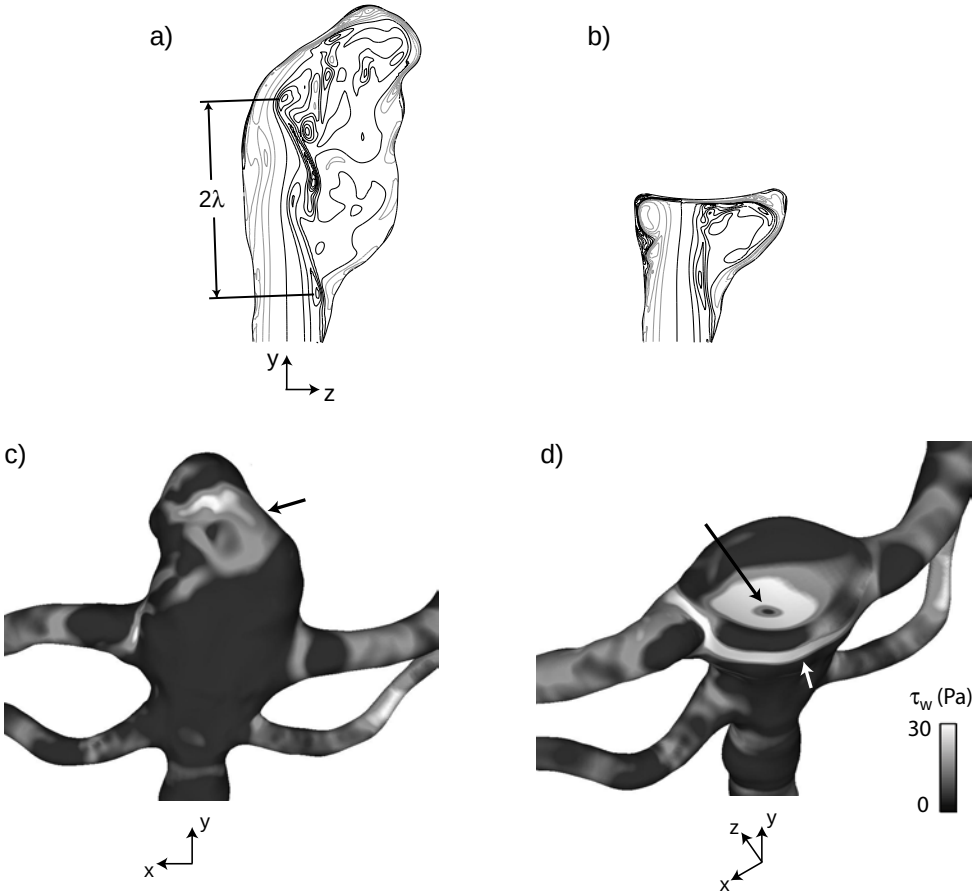

Figure 7. Ortega, *et al.*

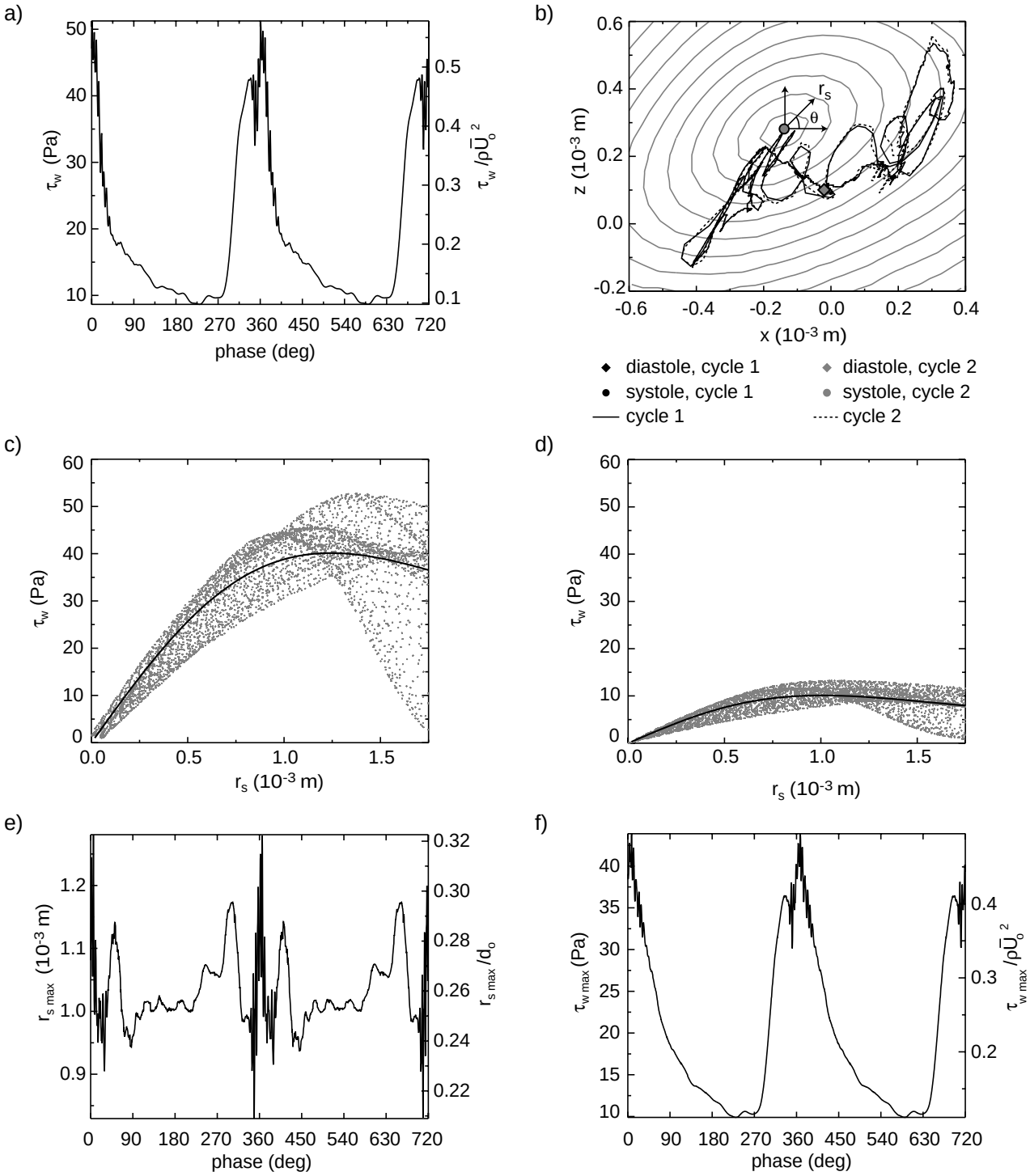

Figure 8. Ortega, *et al.*

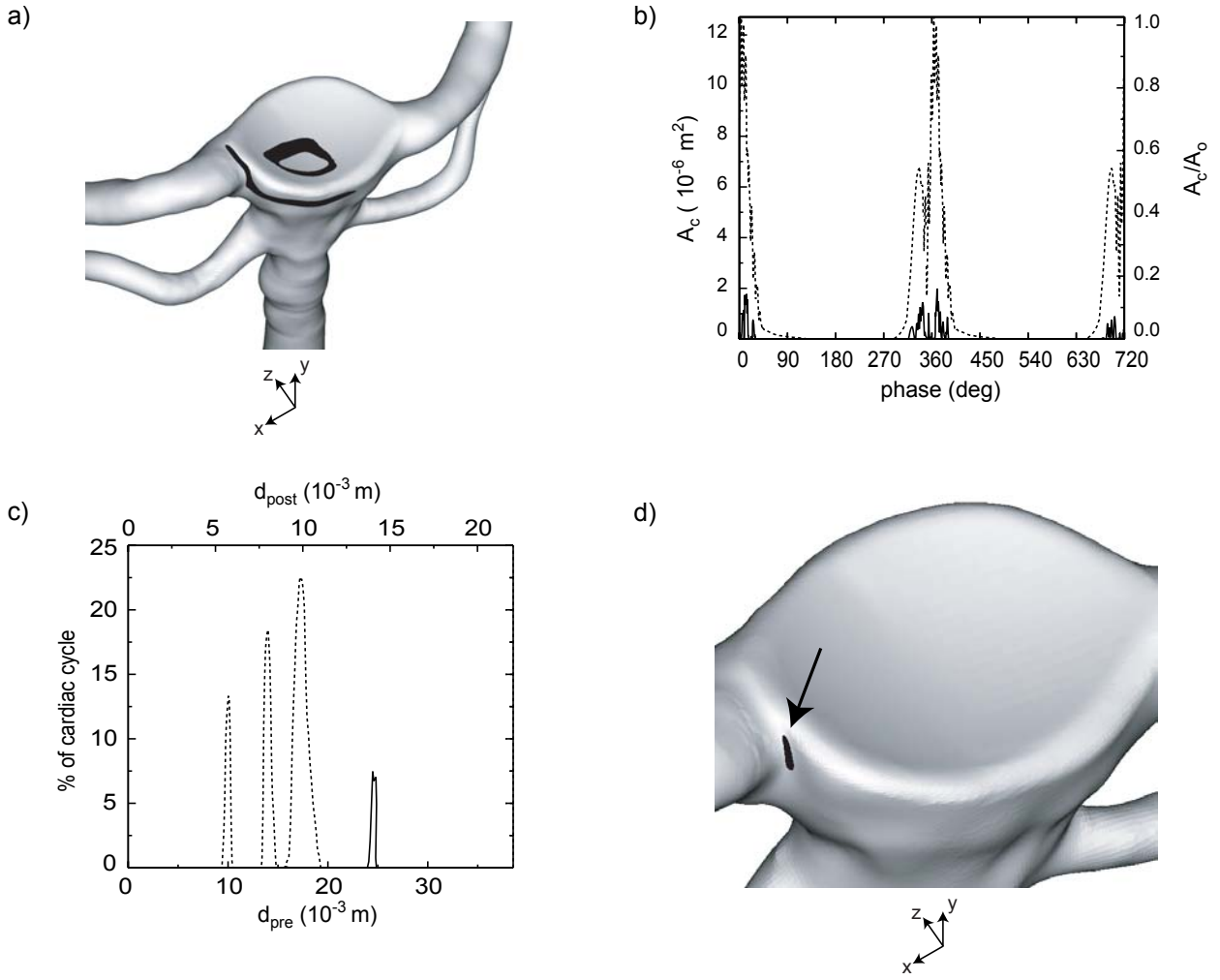

Figure 9. Ortega, *et al.*

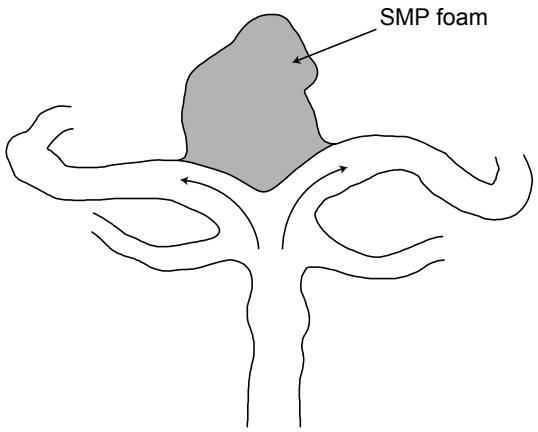

Figure 10. Ortega, *et al.*